A&A 493, L53–L56 (2009)
DOI: 10.1051/0004-6361:200810980
© ESO 2009

Astronomy & Astrophysics

Letter to the Editor

The environment of the fast rotating star Achernar⋆,⋆⋆

II. Thermal infrared interferometry with VLTI/MIDI

P. Kervella[1], A. Domiciano de Souza[2], S. Kanaan[2], A. Meilland[3], A. Spang[2], and Ph. Stee[2]

[1] LESIA, Observatoire de Paris, CNRS UMR 8109, UPMC, Univ. Paris Diderot, 5 place Jules Janssen, 92195 Meudon Cedex, France
e-mail: Pierre.Kervella@obspm.fr
[2] Lab. H. Fizeau, CNRS UMR 6525, Univ. de Nice-Sophia Antipolis, Observatoire de la Côte d'Azur, 06108 Nice Cedex 2, France
[3] Max-Planck-Intitut für Radioastronomie, Auf dem Hugel 69, 53121 Bonn, Germany

Received 17 September 2008 / Accepted 10 December 2008

ABSTRACT

Context. As is the case of several other Be stars, Achernar is surrounded by an envelope, recently detected by near-IR interferometry.
Aims. We search for the signature of circumstellar emission at distances of a few stellar radii from Achernar, in the thermal IR domain.
Methods. We obtained interferometric observations on three VLTI baselines in the N band (8−13 μm), using the MIDI instrument.
Results. From the measured visibilities, we derive the angular extension and flux contribution of the N band circumstellar emission in the polar direction of Achernar. The interferometrically resolved polar envelope contributes 13.4 ± 2.5% of the photospheric flux in the N band, with a full width at half maximum of 9.9 ± 2.3 mas (≈6 $R_\star$). This flux contribution is in good agreement with the photometric IR excess of 10−20% measured by fitting the spectral energy distribution. Due to our limited azimuth coverage, we can only establish an upper limit of 5−10% for the equatorial envelope. We compare the observed properties of the envelope with an existing model of this star computed with the SIMECA code.
Conclusions. The observed extended emission in the thermal IR along the polar direction of Achernar is well reproduced by the existing SIMECA model. Already detected at 2.2 μm, this polar envelope is most probably an observational signature of the fast wind ejected by the hot polar caps of the star.

Key words. stars: individual: Achernar – stars: emission-line, Be – methods: observational – techniques: interferometric

1. Introduction

The southern Be star Achernar (α Eri, HD 10144) has received much interest since its strongly distorted photosphere was resolved by long-baseline interferometry (Domiciano de Souza et al. 2003), with major and minor axes of respectively θ = 2.13 ± 0.05 and 1.51 ± 0.02 milliarcsec (Kervella & Domiciano de Souza 2006, hereafter K06). Due to its extremely fast rotation ($v \sin i \approx 250$ km s^{-1}) and consequent flattening, the von Zeipel effect (von Zeipel 1924) causes the polar caps to be overheated: the polar effective temperature could be higher than 20 000 K, compared to ≲10 000 K at the equator (Jackson et al. 2004; Kanaan et al. 2008, hereafter Ka08). The high radiative pressure at the poles creates a fast polar wind that was detected in the near infrared by K06, where its flux reaches 4.7 ± 0.3% of the photosphere. In addition to this circumstellar envelope (hereafter CSE), Kervella & Domiciano de Souza (2007) discovered a close-in companion of Achernar, of spectral type A1V−A3V (Kervella et al. 2008). In the present Letter, we report new interferometric observations of Achernar in the thermal infrared domain, using the VLTI/MIDI instrument. After a description of our measurements (Sect. 2), we derive the contribution and typical angular scale of the polar CSE of Achernar using a simple Gaussian model and compare them to SIMECA model predictions (Sect. 3).

⋆ Based on observations made with ESO Telescopes at Paranal Observatory under programs 078.D-0295(C), (D) and (E).
⋆⋆ Table 2 is only available in electronic form at http://www.aanda.org

2. Observations

2.1. Instrumental setup and data processing

MIDI (Leinert et al. 2003; Ratzka et al. 2007) is the mid-infrared two-telescope beam combiner of the Very Large Telescope Interferometer (VLTI; Glindemann et al. 2004). This instrument is a classical Michelson interferometer working in the astronomical N band (7.6−13.3 μm). For the reported observations of Achernar, we used a prism with a spectral resolution of $R = \lambda/\Delta\lambda \simeq 30$ to obtain spectrally dispersed fringes. During the observations, the secondary mirrors of the two Unit Telescopes were chopping with a frequency of 2 Hz to properly sample the sky background. Achernar was observed in 2006 and 2007, using three 8.2 m telescope baselines (UT1-UT4, UT1-UT2, and UT3-UT4), and the SCIPHOT mode of MIDI. In this observing mode, the photometry of each telescope is recorded simultaneously with the interferometric signals, allowing a more accurate calibration of the visibilities. The average dates of each observation, with the corresponding projected baseline length B and position angle PA are given in Table 1. Each star or calibrator observation corresponds to a time on target recording interferometric fringes of 3 min, followed by approximately 5 min of photometric calibrations. For the raw data processing, we used two different software packages: MIA developed at the Max-Planck-Institut für Astronomie and EWS developed at the Leiden Observatory (MIA+EWS[1], version 1.5.2) in order to extract the calibrated squared visibilities $V^2(\lambda)$ (Chesneau 2007). We found

[1] http://www.strw.leidenuniv.nl/~nevec/MIDI/index.html

Table 1. Log of the observations of Achernar and its calibrator.

#	*Baseline* / Date	UTC	Target	*B* (m)	*PA* (°)
	UT1-UT4				
A	2006-11-06	01:59:46	α Eri	129.39	48.89
B	2006-11-06	02:26:23	HD 9362	129.66	54.55
C	2006-11-07	00:35:03	α Eri	130.22	32.23
D	2006-11-07	01:05:39	HD 9362	129.93	40.06
	UT1-UT2				
E	2006-11-06	00:32:53	α Eri	52.38	4.94
F	2006-11-06	01:07:56	HD 9362	54.64	10.84
G	2006-11-06	03:15:57	α Eri	49.58	29.69
H	2006-11-06	04:08:42	HD 9362	50.53	35.36
	UT3-UT4				
I	2006-12-07	02:48:10	α Eri	62.46	126.54
J	2006-12-07	03:11:45	HD 9362	61.76	132.33
K*	2007-06-28	07:15:29	HD 9362	39.28	50.04
L*	2007-06-28	07:51:38	α Eri	46.10	52.25

* Due to a photometric instability, #K and #L were rejected.

a good agreement between the results of the MIA and EWS packages within the error bars. In the following we will refer to the results obtained with the EWS package. Our calibrator, δ Phe (HD 9362, G9III), was chosen in the Cohen et al. (1999) catalogue of spectrophotometric standards for infrared wavelengths. δ Phe is located relatively close to Achernar on the sky (8.2°), and is of comparable brightness in the *N* band (9.5 Jy at 12 μm vs. ≈16 Jy for Achernar). It is almost unresolved by the interferometer in the *N* band, with $\theta_{\rm LD} = 2.24 \pm 0.02$ mas (Bordé et al. 2002). The calibrated squared visibilities of Achernar are listed in Table 2. As MIDI operates in the diffraction limited regime of the UTs, the effective field of view diameter is equal to ≈0.26″ at $\lambda = 10\ \mu$m, much larger than the angular size of Achernar and its CSE. An imaging campaign in the *N* band (Kervella & Domiciano de Souza 2007) uncovered a faint companion (Achernar B) located ≈0.3″ away from the star. Considering that the flux contribution of B is only ≈2% of A in the *N* band, we assume in the following that its impact on the MIDI visibilities is negligible compared to their accuracy, and refer to Achernar A simply as "Achernar".

2.2. Visibilities

The calibrated visibilities of Achernar are presented in Fig. 1. One problem we encountered is that the V^2 spectra for our two UT1−UT2 baseline observations #E and #G originally reached "unphysical" values larger than unity. Such a behavior was noticed by Chesneau (2007), and is caused by an incorrect estimation of the κ coefficients that characterize the internal photometric transmission of the instrument. The resulting visibility spectrum is affected by a multiplicative bias larger than unity, uniform with wavelength. We could identify the cause for this behavior in the data sets #F and #H. The derived interferometric transfer function T^2 from these calibrator observations is systematically lower than observation #B of the same calibrator, that was made (in time) in between observations #F and #H. The ratio $\gamma(\#X) = T^2(\#X)/T^2(\#B)$ is respectively $\gamma(\#F) = 0.86 \pm 0.07$ and $\gamma(\#H) = 0.82 \pm 0.03$. As the seeing was stable over all our observations obtained on 2006-11-06 (0.6–0.9″ in the visible), such a variation of T^2 cannot be explained by changing atmospheric conditions. The instrumental cause for this bias on the calibrator V^2 spectrum is not identified, but could be linked to an instrumental polarization problem. Our other observations are apparently free of such a "κ-induced" bias. The fact that we obtain nearly the same V^2 spectrum for two different nights on

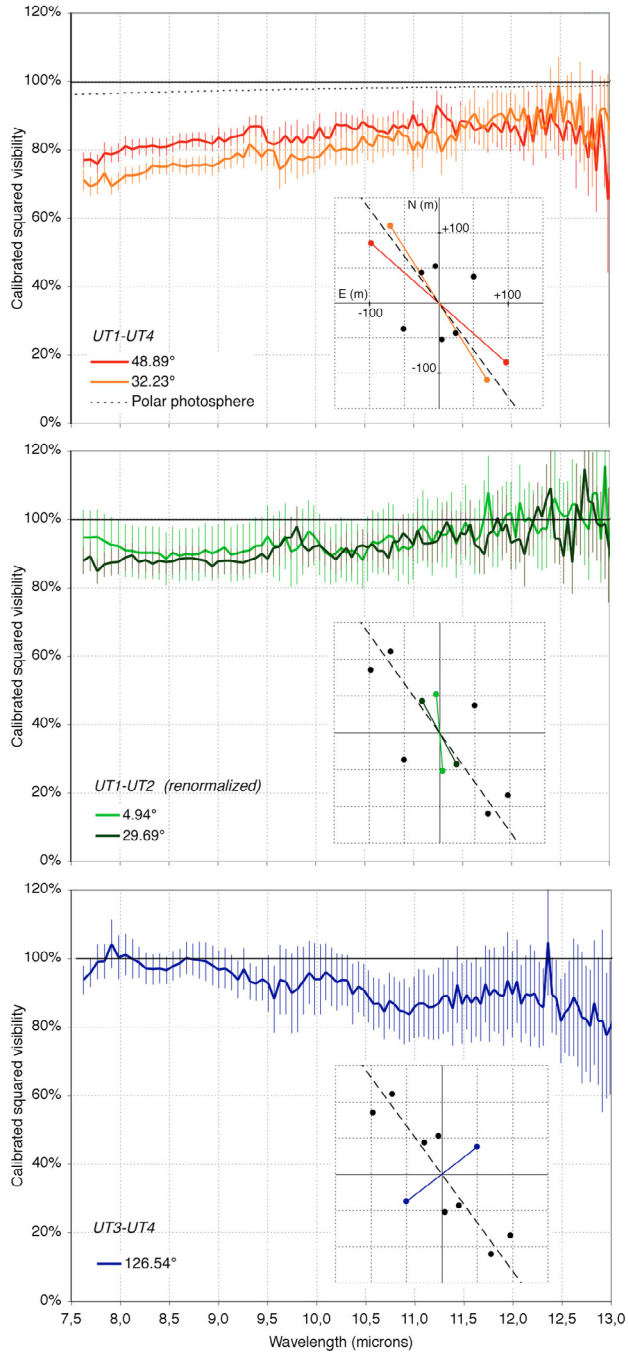

Fig. 1. Squared visibilities of Achernar. The error bars are the statistical dispersion of the V^2 measurements from the EWS software. The position angles of each projected baseline are given in degrees. The inset diagrams show each baseline in the $(\lambda u, \lambda v)$ plane, and the polar direction of Achernar (dashed line). Thanks to the spectral coverage of MIDI, a relatively broad range of spatial frequencies is sampled simultaneously for each baseline (see Fig. 4). The dotted line in the upper plot shows the polar V^2 function of Achernar, for $B = 130$ m. The UT1−UT2 V^2 values were renormalized (see Sect. 2.2 for details).

the UT1−UT4 baseline (Fig. 1, top) gives confidence in their calibration. For this reason, we uniformly multiplied the V^2 spectra obtained on the UT1−UT2 baseline by the relevant γ factors, whose uncertainties are reflected in the V^2 error bars (Fig. 1, middle).

Achernar shows a squared visibility deficit on the longer UT1−UT4 baseline (Fig. 1, top, $B \approx 130$ m), that is almost aligned with the rotation axis of the star. Such a deficit

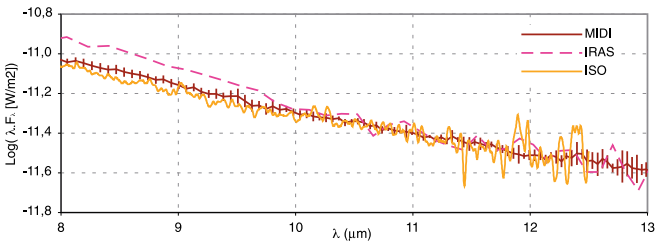

Fig. 2. Absolutely calibrated MIDI spectrum of Achernar, using HD 9362 as a spectrophotometric standard star, with the spectra from IRAS LRS and ISO SWS (PWS processing) superposed.

($\Delta V^2 \approx 20$–30%) can be explained by the presence of a resolved CSE component, as discussed in Sect. 3. The visibilities on the UT3–UT4 baseline along the direction of the equator of the star show almost no resolution. However, the shorter projected baseline length of ≈62 m reduces the sensitivity of the interferometer to moderately extended emission.

2.3. Spectrophotometry

The absolutely calibrated spectrum of Achernar presented in Fig. 2 was obtained by dividing the average MIDI spectrum by the average spectrum of its calibrator HD 9362, and then multiplying the result by the template spectrum from Cohen et al. (1999). The agreement with the IRAS spectrum (Volk & Cohen 1989) is satisfactory, although an excess can be noticed in the IRAS data between 8 and 10 μm, compared to the MIDI and ISO spectra. This could be attributed to a different activity level of the star for these two observations. According to Fig. 14 of Ka08, our MIDI observations were obtained in a state of increasing Hα emission of Achernar, after a minimum occuring around 2000–2002. The IRAS observations took place in 1983, a year during which Achernar was in a decreasing, moderate activity state (Balona et al. 1987). The ISO SWS spectrum (Sloan et al. 2003) was obtained in 1996, when the star was also in a decreasing activity state (Vinicius et al. 2006).

The spectral energy distribution (SED) model presented in Fig. 3 was taken from the database of Castelli & Kurucz (2003) using an average $T_{\rm eff}$ of 15 000 K and $\log g = 3.5$ (Levenhagen & Leister 2006; Lovekin et al. 2006), for solar metallicity. The average angular diameter was set to $\theta_{\rm LD} = 1.79$ mas in order to match the observed broadband photometry in the V band, taken as a fiducial value. We chose this band as the contribution from the CSE is expected to be small in the visible. This value is very close to the arithmetic average of the polar and equatorial angular diameters (1.82 mas) measured by K06. We are aware that this SED model is not physically realistic (it ignores in particular the von Zeipel effect), but Lovekin et al. (2006) showed that the deviation from a rotating star SED is reasonably small. The photometry was taken from Ducati (2002) for the U to N broadband photometry, Thompson et al. (1978) for the UV, ISO (Kessler et al. 2003), IRAS (IPAC 1986), and COBE/DIRBE (Smith et al. 2004) for the IR. We also used the VLT/VISIR photometry obtained by Kervella & Domiciano de Souza (2007), as well as the average flux measured with MIDI between 8 and 12 μm (Fig. 2). As shown in Fig. 3 (bottom), an excess emission of ≈10–20% of the photospheric flux is present around $\lambda = 10\,\mu$m, but not at 25 and 60 μm (IRAS measurements).

3. Extended emission

To estimate the relative flux contribution and spatial extension of the CSE of Achernar, we use the simple model of a uniformly bright photosphere surrounded by a Gaussian CSE, with a full width at half maximum ρ and a flux contribution relatively to the photosphere $\alpha = f_{\rm CSE}/f_\star$. In this model, we assume that the CSE extension is independent of wavelength over the N band. This type of model was already used by K06, and the interested reader is referred to these authors' Sects. 3.3 to 3.5 for details. In the present work, we restrict the fitting process to the polar direction of Achernar, i.e. to the UT1–UT4 and UT1–UT2 baselines, that are approximately aligned (Fig. 1). We fix the photospheric polar angular size to $\theta_{\rm pol} = 1.51$ mas (K06). The adjusted V^2 model is:

$$V^2_{\rm model}(\rho, \alpha, \theta_{\rm pol}, \nu) = \left(\frac{V_\star + \alpha V_{\rm CSE}}{1+\alpha}\right)^2 \quad (1)$$

where the photospheric ($V_\star$) and CSE ($V_{\rm CSE}$) visibilities are:

$$V_\star(\theta_{\rm pol}, \nu) = \left|\frac{2\,J_1(\pi\,\theta_{\rm pol}\,\nu)}{\pi\,\theta_{\rm pol}\,\nu}\right|, \quad V_{\rm CSE}(\rho, \nu) = \exp\left[-\frac{(\pi\,\rho\,\nu)^2}{4\,\ln 2}\right], \quad (2)$$

where ρ is the FWHM of the CSE, and $\nu = B/\lambda$ the spatial frequency of the interferometric measurement. The result of this fit is shown in Fig. 4. The derived polar CSE parameters are a FWHM of $\rho = 9.9 \pm 2.3$ mas and a flux contribution of $\alpha = 13.4 \pm 2.5\%$ relatively to the photosphere, on average over the N band. The reduced χ^2 of the fit is satisfactory at 1.6. The measured CSE flux is comparable to the excess measured photometrically of 10–20% (Sect. 2.3).

Along the equatorial direction, the visibilities obtained on the UT3–UT4 baseline (Fig. 1, bottom) are only marginally different from unity. We can only set an upper limit of ≈5% to the CSE flux contribution at 8 μm and ≈10% at 12 μm in the equatorial direction of the star, at spatial scales larger than 20–30 mas. The possibility still exists that a significant equatorial CSE contribution exists in this direction, but it should then be smaller than ≈10 $R_\star$. A comparison of the photometric infrared excess measured in Sect. 2.3 and the resolved polar CSE flux observed with MIDI also leaves little space for a bright equatorial

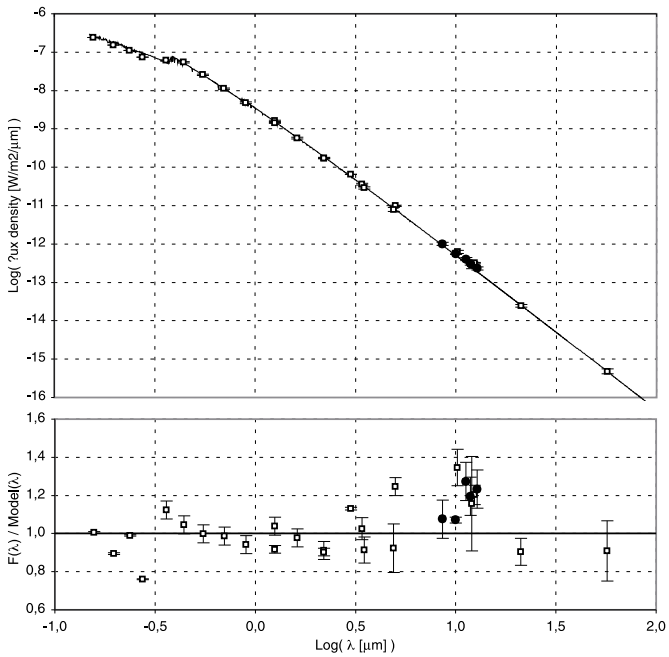

Fig. 3. Spectral energy distribution of Achernar. The open squares are measurements from the literature. The MIDI and VISIR points (Kervella & Domiciano de Souza 2007) are shown as solid dots.

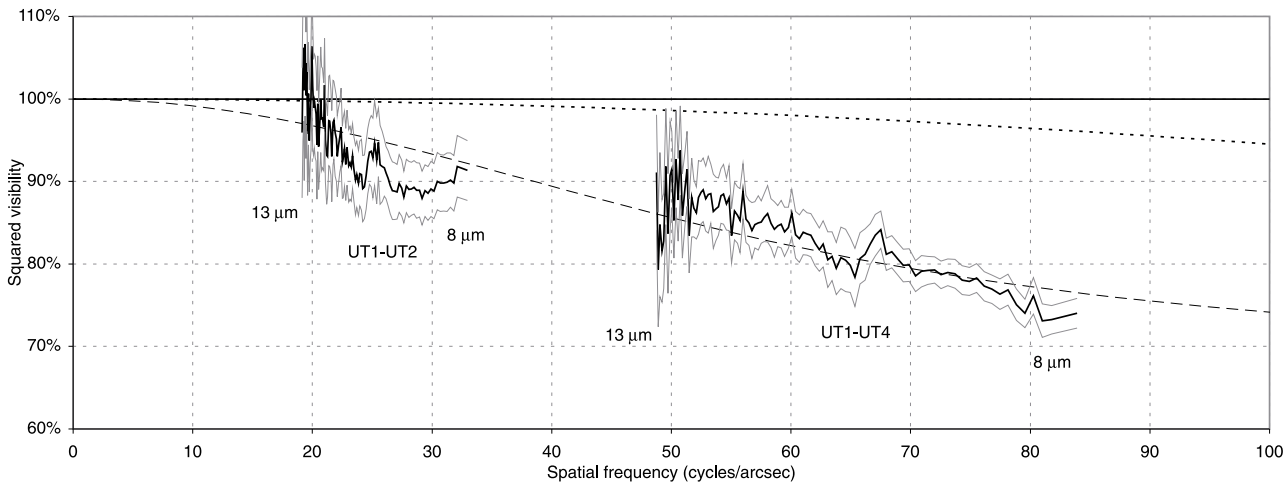

Fig. 4. Observed V^2 values of Achernar and adjusted photosphere+Gaussian envelope model (dashed curve) along the polar direction (separate averages of UT1−UT4 and UT1−UT2 baselines), as a function of spatial frequency. The polar photospheric V^2 is shown as a dotted curve.

component. We can roughly estimate the maximum equatorial CSE emission to ≈5−10% at all spatial scales, in the N band.

For the present discussion, we choose to check the agreement of Ka08's Achernar model with the parameters derived from our Gaussian CSE model fitting, rather than directly fit the SIMECA model to the MIDI data. The reason for this indirect approach is the limited coverage in baseline orientation and length of the MIDI data that make the convergence of the fit difficult. The model of Achernar was computed by Ka08 using the SIMECA code (Stee & Bittar 2001) for their analysis of VLTI/VINCI data. SIMECA has been developed to model the environment of active hot stars. It computes line profiles, spectral energy distributions (SEDs), and intensity maps in lines and the continuum, which can be directly compared to spectroscopic, photometric and high angular resolution observations. The best model of Ka08 for the epoch of VINCI observations (2002−2003) is that of a polar wind with an opening angle of about 20° in the K band (the model parameters are listed in Table 1 of Ka08). From this same SIMECA model, we derive in the N band a half-maximum CSE radius of 6.8 $R_\star$, giving an angular FWHM of ≈10 mas considering the ≈7 $R_\odot$ polar radius of Achernar and its $\pi = 22.68 \pm 0.57$ parallax (ESA 1997). The associated N band flux contribution of the CSE is 11% of the photosphere. The model extension and flux contribution are both in excellent agreement with the results of our MIDI observations (Sect. 3).

The SIMECA model predicts CSE fluxes of ≈2× and ≈11× the photosphere at 25 and 60 μm. Figure 3 shows no such excess in the IRAS photometry. This discrepancy may be due to the low activity of Achernar during IRAS observations, or more probably to inaccuracies of the model in this wavelength range.

4. Conclusion

From new interferometric observations in the thermal infrared domain (8−13 μm), we resolve an extended CSE along the polar direction of Achernar, whose total flux is 13.4 ± 2.5% of the photosphere, with a FWHM of 9.9 ± 2.3 mas (≈6 $R_\star$). This flux contribution is consistent with the photometric infrared excess of 10−20% measured in the same wavelength domain, and with the predictions by the SIMECA model of Ka08. This convergence strengthens the plausibility of the presence of a fast polar wind ejected from the overheated polar caps of the star. According to the scenario proposed by Ka08, Achernar is currently in a disk formation phase. Unfortunately, our limited coverage of the equatorial direction of Achernar with the MIDI data restricts our sensitivity. We could only set an upper flux limit of ≈10% for an extended CSE in this direction. This non-detection is consistent with the K06 results in the K band.

Acknowledgements. We thank Dr. O. Chesneau for his help in the processing of MIDI data, and the referee Dr. D. R. Gies for helpful comments on our manuscript. This research used the SIMBAD and VizieR databases at CDS, Strasbourg (France), and NASA's ADS bibliographic services. We used ISO (an ESA project) and NASA/IPAC Archive data. We received the support of PHASE, the high angular resolution partnership between ONERA, Observatoire de Paris, CNRS, and University Denis Diderot Paris 7.

References

Balona, L. A., Engelbrecht, C. A., & Marang, F. 1987, MNRAS, 227, 123
Bordé, P., Coudé du Foresto, V., Chagnon, G., & Perrin, G. 2002, A&A, 393, 183
Castelli, F., & Kurucz, R. L. 2003, Proc. IAUS, 210, A20 [arXiv:astro-ph/0405087]
Chesneau, O. 2007, New Astron. Rev., 51, 666
Cohen, M., Walker, R. G., Carter, B., et al. 1999, AJ, 117, 1864
Domiciano de Souza, A., Kervella, P., Jankov, S., et al. 2003, A&A, 407, L47
Ducati, J. R. 2002, NASA Ref. Pub., 1294
ESA 1997, The Hipparcos and Tycho Catalogues, ESA SP-1200
Glindemann, A., Albertsen, M., Andolfato, L., et al. 2004, SPIE, 5491, 447
IPAC 1986, IRAS Catalog of Point Sources, v.2.0, Joint IRAS Science W.G.
Jackson, S., MacGregor, K. B., & Skumanich, A. 2004, ApJ, 606, 1196
Kanaan, S., Meilland, A., Stee, Ph., et al. 2008, A&A, 486, 785 (Ka08)
Kervella, P., & Domiciano de Souza, A. 2006, A&A, 453, 1059 (K06)
Kervella, P., & Domiciano de Souza, A. 2007, A&A, 474, L49
Kervella, P., Domiciano de Souza, A., & Bendjoya, Ph. 2008, A&A, 484, L13
Kessler, M. F., Müller, T. G., Leech, K., et al. 2003, ESA SP-1262
Leinert, C., Graser, U., Przygodda, F., et al. 2003, Ap&SS, 286, 73
Levenhagen, R. S., & Leister, N. V. 2006, MNRAS, 371, 252
Lovekin, C. C., Deupree, R. G., & Short, C. I. 2006, ApJ, 643, 460
Ratzka, T., Leinert, C., & Henning, T. 2007, A&A, 471, 173
Sloan, G. C., Kraemer, K. E., Price, S. D., & Shipman, R. F. 2003, ApJS, 147, 379
Smith, B. J., Price, S. D., & Baker, R. I. 2004, ApJS, 154, 673
Stee, Ph., & Bittar, J. 2001, A&A, 367, 532
Thompson, G. I., Nandy, K., Jamar, C., et al. 1978, Catalogue of stellar ultraviolet fluxes (TD1), The Science Research Council, UK
Vinicius, M. M. F., Zorec, J., Leister, N. V., & Levenhagen, R. S. 2006, A&A, 446, 643
Volk, K., & Cohen, M. 1989, AJ, 98, 1918
von Zeipel, H. 1924, MNRAS, 84, 665

Table 2. MIDI squared visibilities of Achernar. The position angle is counted positively East of North ($N = 0°$, $E = 90°$).

Baseline	UT1–UT4	UT1–UT4	UT1–UT2	UT1–UT2	UT3–UT4
Proj. B (m)	129.39	130.22	52.38	49.58	62.46
Pos. Angle (°)	48.89	32.23	4.94	29.69	126.54
λ (μm)	$V^2(\lambda) \pm \sigma$	$V^2(\lambda) \pm \sigma$	$V^2(\lambda) \pm \sigma$	$V^2(\lambda) \pm \sigma$	$V^2(\lambda) \pm \sigma$
7.623	0.770 ± 0.022	0.711 ± 0.031	0.947 ± 0.079	0.879 ± 0.041	0.938 ± 0.042
7.695	0.771 ± 0.022	0.693 ± 0.028	0.946 ± 0.079	0.890 ± 0.042	0.959 ± 0.042
7.767	0.760 ± 0.028	0.703 ± 0.031	0.948 ± 0.081	0.847 ± 0.037	0.991 ± 0.052
7.839	0.791 ± 0.032	0.732 ± 0.030	0.936 ± 0.079	0.867 ± 0.036	0.992 ± 0.051
7.911	0.786 ± 0.023	0.694 ± 0.026	0.925 ± 0.082	0.873 ± 0.039	1.043 ± 0.072
7.982	0.793 ± 0.028	0.708 ± 0.026	0.921 ± 0.077	0.875 ± 0.038	1.005 ± 0.065
8.053	0.812 ± 0.029	0.726 ± 0.025	0.908 ± 0.078	0.888 ± 0.038	1.011 ± 0.062
8.123	0.802 ± 0.028	0.725 ± 0.024	0.906 ± 0.076	0.894 ± 0.039	0.999 ± 0.058
8.194	0.810 ± 0.024	0.729 ± 0.025	0.901 ± 0.076	0.875 ± 0.037	0.988 ± 0.046
8.263	0.809 ± 0.025	0.737 ± 0.025	0.901 ± 0.077	0.881 ± 0.037	0.971 ± 0.045
8.333	0.812 ± 0.024	0.754 ± 0.025	0.901 ± 0.077	0.870 ± 0.036	0.969 ± 0.045
8.402	0.807 ± 0.026	0.751 ± 0.023	0.899 ± 0.077	0.878 ± 0.034	0.971 ± 0.044
8.471	0.809 ± 0.026	0.752 ± 0.024	0.884 ± 0.077	0.876 ± 0.036	0.966 ± 0.040
8.539	0.817 ± 0.024	0.760 ± 0.024	0.902 ± 0.077	0.877 ± 0.036	0.979 ± 0.044
8.607	0.825 ± 0.023	0.754 ± 0.023	0.894 ± 0.076	0.885 ± 0.038	0.986 ± 0.042
8.674	0.824 ± 0.024	0.750 ± 0.023	0.899 ± 0.076	0.887 ± 0.036	1.003 ± 0.047
8.741	0.829 ± 0.021	0.756 ± 0.024	0.896 ± 0.077	0.886 ± 0.035	0.997 ± 0.047
8.807	0.830 ± 0.021	0.754 ± 0.028	0.898 ± 0.079	0.883 ± 0.038	0.996 ± 0.054
8.874	0.825 ± 0.026	0.758 ± 0.027	0.910 ± 0.080	0.879 ± 0.035	0.991 ± 0.057
8.939	0.818 ± 0.025	0.752 ± 0.028	0.899 ± 0.080	0.863 ± 0.034	0.980 ± 0.058
9.004	0.836 ± 0.030	0.761 ± 0.027	0.907 ± 0.080	0.877 ± 0.037	0.968 ± 0.055
9.069	0.824 ± 0.028	0.772 ± 0.028	0.917 ± 0.080	0.878 ± 0.039	0.972 ± 0.058
9.133	0.837 ± 0.027	0.775 ± 0.029	0.896 ± 0.080	0.878 ± 0.036	0.959 ± 0.052
9.197	0.840 ± 0.025	0.790 ± 0.032	0.901 ± 0.082	0.876 ± 0.038	0.938 ± 0.055
9.260	0.846 ± 0.026	0.778 ± 0.030	0.905 ± 0.083	0.872 ± 0.039	0.970 ± 0.060
9.322	0.867 ± 0.030	0.816 ± 0.035	0.910 ± 0.082	0.880 ± 0.038	0.934 ± 0.054
9.385	0.869 ± 0.032	0.800 ± 0.041	0.922 ± 0.083	0.886 ± 0.037	0.928 ± 0.051
9.446	0.867 ± 0.031	0.780 ± 0.040	0.924 ± 0.081	0.897 ± 0.034	0.940 ± 0.060
9.507	0.822 ± 0.040	0.801 ± 0.049	0.950 ± 0.089	0.883 ± 0.038	0.927 ± 0.082
9.568	0.816 ± 0.040	0.798 ± 0.049	0.921 ± 0.090	0.915 ± 0.049	0.882 ± 0.098
9.628	0.823 ± 0.044	0.744 ± 0.059	0.921 ± 0.102	0.919 ± 0.054	0.938 ± 0.100
9.688	0.841 ± 0.042	0.756 ± 0.055	0.950 ± 0.096	0.944 ± 0.046	0.932 ± 0.096
9.747	0.821 ± 0.051	0.788 ± 0.056	0.905 ± 0.101	0.947 ± 0.062	0.899 ± 0.116
9.806	0.840 ± 0.047	0.775 ± 0.060	0.913 ± 0.104	0.979 ± 0.059	0.911 ± 0.125
9.864	0.819 ± 0.044	0.770 ± 0.045	0.934 ± 0.097	0.923 ± 0.056	0.935 ± 0.099
9.922	0.838 ± 0.036	0.780 ± 0.051	0.965 ± 0.091	0.908 ± 0.049	0.960 ± 0.092
9.980	0.834 ± 0.051	0.777 ± 0.045	0.952 ± 0.088	0.920 ± 0.044	0.940 ± 0.106
10.037	0.866 ± 0.041	0.782 ± 0.038	0.926 ± 0.091	0.923 ± 0.044	0.940 ± 0.103
10.093	0.836 ± 0.032	0.799 ± 0.045	0.904 ± 0.089	0.910 ± 0.046	0.961 ± 0.083
10.149	0.834 ± 0.035	0.816 ± 0.042	0.893 ± 0.084	0.894 ± 0.043	0.946 ± 0.086
10.205	0.875 ± 0.036	0.795 ± 0.039	0.900 ± 0.085	0.883 ± 0.045	0.931 ± 0.083
10.260	0.871 ± 0.040	0.802 ± 0.033	0.917 ± 0.089	0.900 ± 0.049	0.938 ± 0.075
10.315	0.873 ± 0.033	0.804 ± 0.048	0.903 ± 0.087	0.917 ± 0.044	0.936 ± 0.075
10.369	0.862 ± 0.037	0.800 ± 0.046	0.909 ± 0.089	0.888 ± 0.044	0.897 ± 0.088
10.423	0.860 ± 0.035	0.810 ± 0.049	0.897 ± 0.088	0.920 ± 0.045	0.918 ± 0.074
10.477	0.883 ± 0.035	0.840 ± 0.050	0.880 ± 0.084	0.923 ± 0.049	0.908 ± 0.077
10.530	0.870 ± 0.029	0.818 ± 0.048	0.913 ± 0.096	0.918 ± 0.042	0.890 ± 0.076
10.582	0.868 ± 0.038	0.810 ± 0.049	0.935 ± 0.091	0.927 ± 0.044	0.869 ± 0.077
10.635	0.853 ± 0.035	0.843 ± 0.051	0.928 ± 0.091	0.907 ± 0.047	0.869 ± 0.071
10.687	0.854 ± 0.028	0.838 ± 0.059	0.938 ± 0.093	0.908 ± 0.050	0.845 ± 0.079
10.739	0.847 ± 0.051	0.836 ± 0.045	0.952 ± 0.094	0.886 ± 0.050	0.877 ± 0.082
10.790	0.872 ± 0.040	0.827 ± 0.044	0.948 ± 0.095	0.934 ± 0.052	0.868 ± 0.079
10.841	0.865 ± 0.051	0.857 ± 0.046	0.907 ± 0.088	0.934 ± 0.050	0.850 ± 0.084
10.892	0.870 ± 0.038	0.843 ± 0.045	0.920 ± 0.082	0.959 ± 0.055	0.845 ± 0.097
10.942	0.862 ± 0.029	0.839 ± 0.052	0.913 ± 0.104	0.944 ± 0.055	0.838 ± 0.079
10.993	0.903 ± 0.040	0.797 ± 0.058	0.921 ± 0.096	0.926 ± 0.049	0.858 ± 0.089
11.042	0.870 ± 0.035	0.825 ± 0.046	0.965 ± 0.095	0.967 ± 0.054	0.871 ± 0.099
11.092	0.876 ± 0.042	0.805 ± 0.057	0.980 ± 0.104	0.928 ± 0.047	0.870 ± 0.098
11.141	0.849 ± 0.033	0.851 ± 0.048	0.959 ± 0.099	0.928 ± 0.051	0.858 ± 0.093
11.190	0.854 ± 0.034	0.855 ± 0.053	0.930 ± 0.094	0.931 ± 0.058	0.859 ± 0.096
11.239	0.931 ± 0.042	0.845 ± 0.055	0.967 ± 0.096	0.936 ± 0.061	0.869 ± 0.104
11.288	0.912 ± 0.048	0.793 ± 0.066	0.954 ± 0.094	0.964 ± 0.064	0.891 ± 0.110
11.336	0.892 ± 0.044	0.827 ± 0.055	0.955 ± 0.098	0.993 ± 0.054	0.891 ± 0.106

Table 2. continued.

Baseline	UT1–UT4	UT1–UT4	UT1–UT2	UT1–UT2	UT3–UT4
Proj. B (m)	129.39	130.22	52.38	49.58	62.46
Pos. Angle (°)	48.89	32.23	4.94	29.69	126.54
λ (μm)	$V^2(\lambda) \pm \sigma$	$V^2(\lambda) \pm \sigma$	$V^2(\lambda) \pm \sigma$	$V^2(\lambda) \pm \sigma$	$V^2(\lambda) \pm \sigma$
11.384	0.885 ± 0.042	0.843 ± 0.062	0.982 ± 0.097	0.960 ± 0.060	0.853 ± 0.108
11.432	0.842 ± 0.040	0.826 ± 0.060	0.927 ± 0.099	0.934 ± 0.067	0.924 ± 0.112
11.480	0.885 ± 0.056	0.875 ± 0.055	0.959 ± 0.093	0.960 ± 0.062	0.869 ± 0.118
11.528	0.882 ± 0.036	0.863 ± 0.065	0.991 ± 0.109	0.955 ± 0.064	0.895 ± 0.103
11.575	0.880 ± 0.047	0.889 ± 0.058	0.962 ± 0.095	0.985 ± 0.066	0.872 ± 0.118
11.622	0.858 ± 0.038	0.907 ± 0.068	0.936 ± 0.097	0.925 ± 0.058	0.888 ± 0.116
11.669	0.863 ± 0.049	0.876 ± 0.049	0.948 ± 0.109	0.916 ± 0.071	0.868 ± 0.108
11.716	0.870 ± 0.050	0.863 ± 0.060	1.004 ± 0.110	0.897 ± 0.058	0.926 ± 0.112
11.763	0.851 ± 0.059	0.876 ± 0.070	1.078 ± 0.107	0.956 ± 0.067	0.893 ± 0.134
11.809	0.877 ± 0.041	0.893 ± 0.073	0.966 ± 0.105	0.967 ± 0.062	0.910 ± 0.122
11.856	0.867 ± 0.060	0.901 ± 0.074	0.951 ± 0.091	1.003 ± 0.081	0.894 ± 0.111
11.902	0.851 ± 0.051	0.907 ± 0.062	0.987 ± 0.109	0.965 ± 0.077	0.890 ± 0.145
11.948	0.894 ± 0.044	0.885 ± 0.079	1.012 ± 0.097	0.986 ± 0.085	0.936 ± 0.143
11.994	0.851 ± 0.057	0.922 ± 0.051	1.018 ± 0.092	0.929 ± 0.078	0.896 ± 0.126
12.039	0.871 ± 0.057	0.890 ± 0.072	0.947 ± 0.094	0.938 ± 0.062	0.934 ± 0.121
12.085	0.838 ± 0.043	0.886 ± 0.047	1.047 ± 0.111	0.941 ± 0.068	0.869 ± 0.112
12.130	0.810 ± 0.043	0.925 ± 0.059	0.993 ± 0.094	0.896 ± 0.092	0.896 ± 0.113
12.175	0.901 ± 0.070	0.860 ± 0.065	1.003 ± 0.105	0.961 ± 0.069	0.892 ± 0.147
12.220	0.823 ± 0.067	0.845 ± 0.060	0.988 ± 0.096	0.992 ± 0.080	0.898 ± 0.125
12.265	0.903 ± 0.059	0.928 ± 0.071	0.957 ± 0.102	1.038 ± 0.069	0.866 ± 0.125
12.310	0.919 ± 0.060	0.862 ± 0.065	0.973 ± 0.123	1.007 ± 0.066	0.858 ± 0.112
12.355	0.844 ± 0.068	0.872 ± 0.077	0.972 ± 0.115	1.061 ± 0.100	1.048 ± 0.155
12.399	0.907 ± 0.082	0.967 ± 0.073	1.035 ± 0.094	1.092 ± 0.111	0.895 ± 0.110
12.443	0.877 ± 0.072	0.878 ± 0.069	1.061 ± 0.140	0.942 ± 0.071	0.886 ± 0.109
12.487	0.865 ± 0.082	0.989 ± 0.083	1.021 ± 0.098	0.942 ± 0.074	0.818 ± 0.123
12.530	0.827 ± 0.057	0.879 ± 0.078	1.008 ± 0.100	0.890 ± 0.079	0.842 ± 0.117
12.574	0.886 ± 0.058	0.943 ± 0.076	1.009 ± 0.102	1.004 ± 0.078	0.855 ± 0.138
12.617	0.877 ± 0.094	0.938 ± 0.091	1.043 ± 0.131	0.873 ± 0.091	0.887 ± 0.171
12.660	0.816 ± 0.129	0.858 ± 0.088	1.042 ± 0.113	1.044 ± 0.120	0.863 ± 0.178
12.702	0.871 ± 0.109	0.965 ± 0.092	1.013 ± 0.116	0.996 ± 0.102	0.828 ± 0.192
12.745	0.841 ± 0.088	0.815 ± 0.077	0.987 ± 0.121	1.146 ± 0.127	0.825 ± 0.155
12.787	0.777 ± 0.111	0.855 ± 0.075	0.969 ± 0.146	1.052 ± 0.164	0.804 ± 0.164
12.828	0.893 ± 0.141	0.803 ± 0.111	1.075 ± 0.113	1.049 ± 0.146	0.872 ± 0.182
12.869	0.739 ± 0.120	0.848 ± 0.085	1.078 ± 0.130	0.988 ± 0.109	0.818 ± 0.187
12.910	0.905 ± 0.099	0.917 ± 0.100	0.940 ± 0.124	0.979 ± 0.102	0.818 ± 0.266
12.950	0.806 ± 0.117	0.923 ± 0.083	1.157 ± 0.151	0.988 ± 0.163	0.775 ± 0.184
12.990	0.655 ± 0.213	0.892 ± 0.130	0.944 ± 0.123	0.926 ± 0.168	0.799 ± 0.195
13.030	0.783 ± 0.175	0.813 ± 0.087	0.808 ± 0.150	0.851 ± 0.140	0.823 ± 0.209